Research Article
Vol. 1, No. 4 | 15 Dec 2018 | OSA CONTINUUM 1215
OSA CONTINUUM

Quantitative label-free technique for morphological evaluation of human sperm—a promising tool in semen evaluation

PRAVEEN KUMAR POOLA,[1] VARSHINI JAYARAMAN,[2] K. CHAITHANYA,[3] DURGA RAO,[3] AND RENU JOHN[1*]

[1]*Department of Biomedical Engineering, Indian Institute of Technology Hyderabad, Kandi, Telangana-502285, India*
[2]*Department of Animal Biology, School of Life sciences, University of Hyderabad, Gachibowli, Hyderabad, Telangana –500046, India*
[3]*Oasis Centre for Reproductive Medicine, Hyderabad, Telangana-500034, India*
**renujohn@iith.ac.in*

Abstract. We present results from non-interferometric quantitative phase imaging (QPI) for thickness estimation and morphological analysis of human spermatozoa. QPI along with algorithms for image processing enable localization and quantification of subcellular structures of spermatozoa, including the acrosomal, nuclear, mid-piece, and tail regions. This approach based on the transport of intensity equation (TIE) using a simple brightfield microscope renders quantitative phase image with nanometric depth sensitivity, allowing the precise subcellular structural resolution of human spermatozoa. We demonstrate the potential of TIE in real-time phase imaging and the morphological analysis of spermatozoa. We first calibrate the TIE using microbeads and a standard phase target of known dimensions. Image processing for quantitative volume estimation of nuclei and acrosomal regions is carried out on the reconstructed quantitative phase images. We also apply a Hilbert transform-based image processing algorithm to the retrieved phase for visualization of vacuoles present on the sperm head.

1. Introduction

Semen analysis is routinely carried out in humans as a diagnostic tool in infertility investigations and for male reproductive health assessment [1–5]. The vital parameters for the assessment of semen quality and fertility are spermatozoa concentration, motility, and morphology [6]. Morphological abnormalities of spermatozoa are the most common and important indicators that lead to poor outcomes from Intra-Uterine Insemination (IUI) leading to male infertility [7]. As the morphology of a sperm cell plays a critical role in its fertilizability, there is a growing interest in understanding and quantifying sperm morphology and its associated defects. In fact, in various procedures for Assisted Reproduction Technology (ART) like *In-Vitro* Fertilization (IVF) [8], Intra Cytoplasmic Sperm Injection (ICSI) [9], and Intracytoplasmic Morphologically Selected Sperm Injection (IMSI) [10,11], assessment and characterization of sperm defects is very important in the selection of best spermatozoa [12,13].

In a routine andrological evaluation, human spermatozoa undergo a cumbersome process of fixing, staining before they are analysed under an optical microscope [14]. The optical translucency of biological cells, coupled with little or no contrast necessitates the use of vital dyes for bright field microscopy, thereby rendering the sperm unusable for clinical use. The present procedures for characterization of spermatozoa are tedious, time consuming and destructive in nature. Optical techniques such as Zernike phase contrast microscopy and differential interferential contrast microscopy [15–17] are helpful in a qualitative visualization of phase, though not capable of quantifying the parameters such as thickness and volume.

#335476 https://doi.org/10.1364/OSAC.1.001215
Journal © 2018 Received 18 Jun 2018; revised 31 Oct 2018; accepted 31 Oct 2018; published 30 Nov 2018

OSA CONTINUUM

Quantitative Phase Microscopy (QPM) techniques such as Digital Holographic Microscopy [18–24], Fourier Phase Microscopy [25], Hilbert Phase Microscopy [26], Diffraction Phase Microscopy [27], Spatial Light Interference Microscopy [28], Quadriwave Lateral Shear Interferometry [29], Gradient Field Microscopy [30], Gradient light Interference Microscopy [31], could render the 3-D morphology of sperms in a non-destructive and label-free manner. Retrieval of phase image and surface morphology of live samples from quantitative phase microscopy will be a paradigm shift in the treatment practice for assisted reproductive techniques [18–22]. However, quantitative phase imaging techniques that are based on interferometry principles would require vibration isolation platforms, complicated experimental set-ups, expensive coherent light sources, and heavy computational support, which makes them non-attractive for practical clinical applications.

Transport of Intensity Equation (TIE) is a non-interferometric quantitative phase imaging technique that is well-suited for this application due to its simplicity in experimental set-up and minimal computational requirements. TIE can be easily realized on a regular brightfield microscope with white light illumination. The phase image reconstructions of the object under study is possible using TIE by recording two defocus images and one in-focus image along the optical axis without the use of any phase unwrapping algorithms [32]. By exploiting a non-coherent white light source or a partially coherent light source [33–37], TIE is capable of reconstructing the thickness of the sample with nanometric depth precisions and high signal to noise ratio (SNR) [38]. TIE has been successfully implemented in many fields such as transmission electron microscopy (TEM) [39,40], and in X-ray imaging [41].

In this paper, we propose TIE for quantitative phase imaging of live sperm cells and its morphological analysis. Imaging of semen sample have been quite challenging and the previously reported works in imaging sperm cells suffered from accuracy, and inability to reveal the structural morphology of the cells [18–21]. Using TIE, we quantify the spermatozoa parameters like width, length, height, area, and volumes of the acrosomal region, nucleus and the head. We also highlight here, the unique strength of TIE imaging in providing morphological information related to DNA content of sperm cells and identifying anomalies associated with the sperm cells (like vacuoles) as per WHO standards [14] using Hilbert transform technique [42]. These are very critical parameters in selecting a fertile sperm in an IVF procedure. This imaging technique will be highly promising for 3-D volume estimation of sperm cells and characterization of sperm morphology with nanometric depth sensitivity without any preprocessing. Since it employs totally incoherent light, this is free of vibration effects and other problems that arise due to use of coherent light.

2. Principle

The idea of relating object intensity measurements to its phase was proposed by Teague in 1983 [43,44]. A plane wave travelling through a transparent phase object gets modulated by the object thickness and undergo a phase change. The quantitative phase of the object modulations can be reconstructed by recording one in-focus and two defocused intensities of the object along the optical axis. A scalar field $U(r_\perp, z)$ at a plane can be represented its amplitude and phase as

$$U(r_\perp, z) = \sqrt{I(r_\perp, z)}\exp(i\varphi(r_\perp, z)) \tag{1}$$

where $I(r_\perp, z)$ is the intensity and $\varphi(r_\perp, z)$ is the spatial distribution of phase of the object. Under the paraxial approximation, TIE relates the first order derivative of axial intensity measurements to the phase at the object plane in the Fresnel region [44,45],

$$\nabla_\perp.(I(r_\perp, z)\nabla_\perp\varphi(r_\perp, z)) = -\frac{2\pi}{\lambda}\frac{dI(r_\perp, z)}{dz} \tag{2}$$

where λ is the spectrally weighted mean wavelength, $\nabla_{\perp}$ is the spatial gradient operator.

With the knowledge of intensity measurements, Eq. (2) relates the measured intensities to the two-dimensional phase distribution in the Fresnel region. A detailed description of TIE formalism can be found in the cited references [42–47]. By following Teague's assumption [46], a formal solution to retrieve the phase $\varphi(r_{\perp},z)$ of an object from Eq. (2) is given as

$$\varphi(r_{\perp},z)=\nabla^{-2}\left[\nabla.\left[\frac{1}{I(r_{\perp},z)}\nabla\left[\nabla^{-2}\left(-\frac{2\pi}{\lambda}\frac{\partial I(r_{\perp},z)}{\partial z}\right)\right]\right]\right] \tag{3}$$

where ∇^{-2} is the inverse Laplacian operator.

By using Fourier transforms method [47], Eq. (3) can be solved on a Matlab^{TM} platform and the retrieved solution is subject to boundary constraints. So while computing phase, it is assumed that intensity is strictly positive. However, the reconstructed phase is prone to errors [48,49], due to the presence of various optical aberrations, phase noise and environmental vibrations. An aberration compensation algorithm has been used in the present study. Using the user-defined sampling points, the algorithm estimates unknown aberrations in the background of the reconstructed phase image. After estimating the aberrations, the image can be corrected by subtracting the estimated aberrations from the reconstructed phase image. The aberration-corrected phase can be converted into object's thickness map with the help of the Eq. (4).

$$t(x,y,z)=\frac{\lambda\Delta\varphi}{2\pi\Delta n} \tag{4}$$

where $\Delta n=n_0-n_m$ is the difference in refractive index between the object (n_0) and its surrounding medium (n_m), $\Delta\varphi=\varphi_0-\varphi_m$ is the phase difference between the object and its background.

2.1 Aberration correction procedure

When the defocus distance between the images along the optical axis is not sufficient, then the final retrieved phase will be corrupted with low frequency artefacts popularly known as cloudy artefacts in TIE. To alleviate the problem of low frequency artefacts, there exists a number of techniques in the literature using stack of more than 11 images along the optical axis [47,50–54]. In this manuscript, we have used a polynomial fitting method as a solution to remove these low frequency artefacts in the retrieved TIE phase image instead of using more images. Consider $\varphi_A(r)$ is the aberration and $\varphi(r)$ is retrieved TIE phase. The aberration can be estimated by polynomial as

$$\varphi_A(r)=\sum_{i=j=0}^{i+j=N}C_{ij}x^i y^j \tag{5}$$

where $C_{i,j}$ are the polynomial coefficients, N is the polynomial order (N = 20 was considered).

The discretized and weighted version of the phase distribution $\varphi(r)$ is $\sum_k W_k\varphi_k$. The coefficients are calculated from the weighted captured phase $\varphi(r)$. Instead of direct filtering, a Low pass filter (LPF) is obtained from low order polynomials, that performs a low pass filtering operation on the input phase data. The calculated aberrations are then subtracted from the actual phase to get the noise-free phase.

OSA CONTINUUM

3. Materials

Characterization of quantitative phase microscopy using TIE was carried out using microbeads (Life Technologies, 4.0 μm) with a known refractive index of 1.68 and were suspended in distilled water (n_{med} = 1.33). Live spermatozoa samples were obtained from Oasis Centre for Reproductive Medicine, Hyderabad, as per approvals from the Institutional Ethical Committee (UH/IEC/2014/114). Following explicit written informed consent, seminal plasma was collected in a wide mouthed, sterile non-toxic container, in a room provided specifically for the purpose. Routine semen analysis was performed after liquefaction according to WHO criteria [14]. The studies were carried out under ambient conditions ensuring the health of the spermatozoa as per WHO guidelines. A part of the sample was utilized for sperm imaging by TIE. All samples were kept in a temperature-regulated chamber and analysed within few hours of collection. The refractive index of sperm cell is considered constant as 1.35 [19,20] and was suspended in an isotonic medium (PBS) of refractive index 1.33. In the current work, the sperms were slowed down to reduce its motility while imaging using clinically approved agents as per standard protocols. We use a drop of PVP (Polyvinylpyrrolidone) with the PBS solution to slow down the spermatozoa.

4. Experimental methods

TIE was performed on a regular inverted bright field microscope (Carl Zeiss Axio-observer). Initially, micro beads were imaged using a tungsten halogen light which is a broad band light source with a center wavelength $\lambda = 550\ nm$ and a CCD camera (1040 X 1388 pixels, pixel size: 6.45 μm) was used for recording three through-focus images along the optical axis separated by a defocus distance of ± 1 μm using the z-stacking feature of the microscope. An aberration-corrected microscope objective (63X, 1.4 NA) was employed for imaging both the microbeads and sperm cells. The calibrated algorithm along with the same experimental set-up have been used for imaging sperm cells.

We have used 63X (1.4NA) objective to image 4 μm sized beads. In case of TIE, the phase of the modulated wave is assumed to be slow-varying and paraxial approximation holds. But, a microscope is a non-paraxial system. In TIE, we are calculating the phase of the magnified image (at the imaging plane), and not the object. Hence, the assumption of paraxiality is a reasonable one. This has been reported in landmark works reported in TIE before [46,51]. The effective NA at the image plane is $NA_{image} \approx NA_{obj} / M$ = 0.02 (for 63X, NA = 1.4) and 0.03 (for 10X, NA = 0.3).

5. Results and discussion

We chose microbeads of known size (4 μm) as standard objects to image and characterize the retrieved phase for further validations. The calibration method involves choosing an optimum defocus distance that minimises the error in calculated phase for an objective lens with a particular numerical aperture. We employ the same defocus distance and algorithm for retrieving the phase of an unknown object. Three defocused intensity recordings [Fig. 1(a)–1(c)] of microbeads are used to retrieve the phase using TIE principle. From these recorded images, 1st derivative of the intensity is computed using finite difference method and is shown in Fig. 1(d). Figure 1(e) shows the reconstructed phase image of the microbeads. A zoom-in depth view of the region marked in Fig. 1(e) is shown in Fig. 1(f). Figure 1(g) shows the retrieved thickness profile of the microbeads across the sample. The microbeads were found to have an average size of 4 ± 0.1 μm. which is in quite agreement with the known size. It has been reported that for samples with width to thickness ratio equal to around 1, the phase reconstructions using the technique employed here will produce errors in the final reconstructed image [48,49]. Hence we expect a certain percent of error in the measurement of thickness of spherical objects such as microbeads. We chose 1 μm defocus distance as an optimum defocus distance for this particular NA and magnification (63X, 1.4 NA). However,

OSA CONTINUUM

for samples with variable width and thicknesses ratio like the sperm cells used in this study, results are expected to be more accurate in comparison to the spherical micro-beads. The choice of defocus distance is an important parameter in getting high fidelity reconstruction. We recorded a stack of images at various defocus distances and applied the reconstruction algorithm for each defocus distance. The range of defocus distances for best phase reconstructions can be chosen from the graph plotted in Fig. 1(h). From the Fig. 1(h), we can see that the graph has a constant phase region from 1 to 5 µm defocus distance with least error in phase. As the reconstructed phase values have low errors over a defocus distance range of 1-5µm [Fig. 1(h)], we used these range of values as defocus distances for the subsequent experiments.

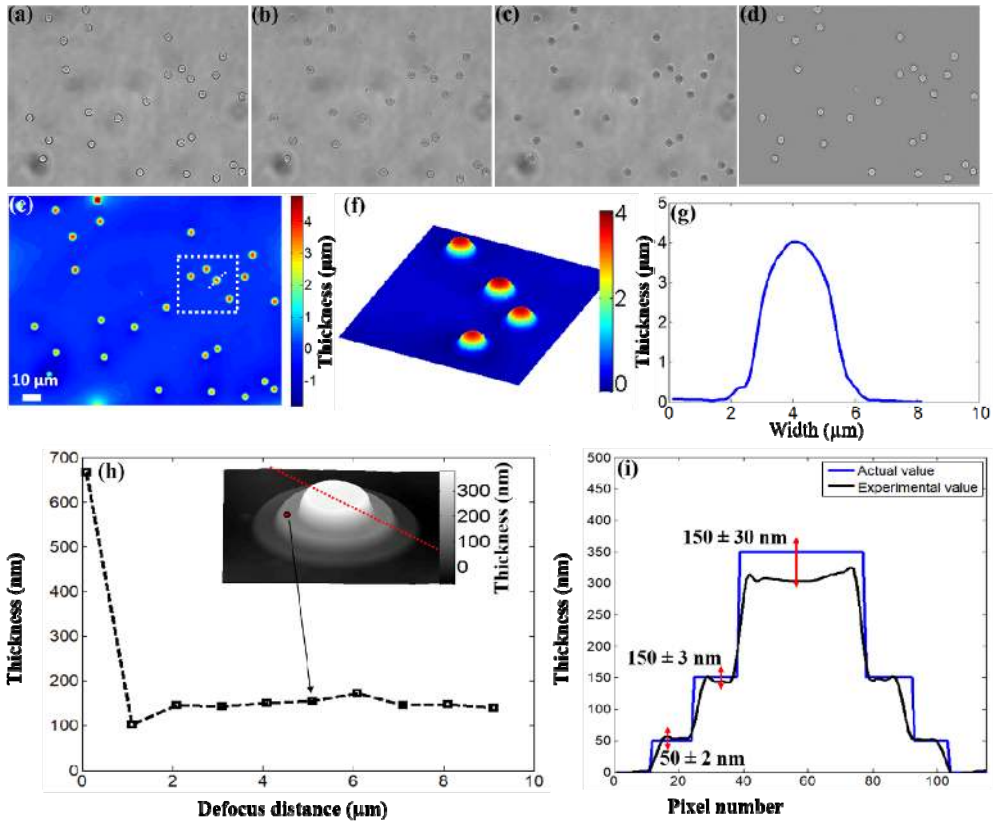

Fig. 1. Reconstruction of phase image of microbeads in brightfield mode. (a-c) Brightfield images captured using the experimental set-up. (a) Image with a defocus of + 1 µm (b) Image in focus (c) Image with a defocus of −1 µm (d) 1st derivative approximation (dI/dz) (e) Aberration-corrected phase image with the color bar showing thickness in µm (f) 3D view of the microspheres. (g) Corresponding line profile from the selected white box portion shown in fig. (e). (h) Plot of phase vs defocus distance for different phase targets with varied thickness (i) graph of actual value vs experimental thickness values for the standard phase target.

To illustrate the accuracy of the phase measurements, we carried out TIE imaging with the set of imaging targets as described below. We imaged a standard phase target (Benchmark Technologies QPM Target) having features of 50 nm (ring width = 1.5 µm), 150 nm (ring width = 1 µm), and, 350 nm (ring width = 3 µm) thicknesses using a microscope objective of 10 X: NA = 0.3. First we calibrated the system to find an optimum defocus distance (5 µm) using the procedure explained above and was shown in Fig. 1(h). The results show an accuracy of ~ ± 3 nm for the heights 50 nm and 150 nm. The error goes to ~9% (~ ± 30) nm

or a height of 350 nm. We believe that this error happens because the T/W ratio approaching 1 at the top of the object. Please refer to Fig. 1(h) for the reconstructed image and its profile on Fig. 1(i).

5.1 Sperm head morphology and Thickness estimation

After the characterization of the system using microbeads and the standard phase target, we performed experiments on live spermatozoa. As explained before, we captured three images; one in-focus and two defocused ones for accurate phase reconstructions. These intensity recordings [Fig. 2(a)–2(c)] are used to retrieve the phase image of sperm cells. First derivative is computed w.r.t to z-axis using finite difference method. Figure 2(d) reveals the reconstructed phase image of the sperm cells. Figure 2(f), 2(g) shows the quantitative phase of the spermatozoon rendered across the cell along the lines AA', BB', CC' and DD' from the phase plot shown in Fig. 2(e). These profiles show a point by point quantitative value of the phase shift resulting from the spermatozoa structure.

Sperm head comprises of two significant parts namely, the nucleus and the acrosome that differs from each other due to their concentration and composition of proteins, nucleic acids and other components [22,55]. The acrosomal part contains an array of hydrolytic enzymes essential for digesting the zona pellucida during penetration of the oocyte, whereas the nucleus part comprises of DNA related proteins, enzymes, and lipids [56]. The results from this technique accurately show the characteristic composition of nucleus and acrosomal region of spermatozoon [Fig. 3(a)]. Quantitative phase shift information from TIE was employed for thickness assessment of sperm head.

In total, 1400 spermatozoa were analyzed from seven subjects. About 200 spermatozoa from each subject were specifically assessed for nine primary parameters with respect to morphology of the sperm head (length, width, perimeter, area, volume estimation of head, acrosome and nucleus, and number and size of vacuoles present within sperm head). We have tabulated the mean values of spermatozoon parameters such as length, width, perimeter, thickness, area, volume, and volumetric distribution of the acrosome and nucleus of the sperm head in Table 1. The average thicknesses of the acrosomal and nuclear compartments is a crucial parameter to know the reason for infertility and was measured for each sperm by segmenting the spermatozoa [57]. The maximal thickness of the nuclear part was 1.25 ± 0.26 μm, and the average acrosome thickness was 370 ± 70 nm. All these parameters are comparable and within the known ranges reported in literature [14,22,55].

Table 1. Evaluated Spermatozoa Parameters

Parameters	Mean value	Range
Length	4.1 ± 0.6 μm	2.2–5.1 μm
Width	3.5 ± 0.5 μm	2.2–4.8 μm
Perimeter	12.5 ± 1.5 μm	8.5–18.5 μm
Thickness	0.6 ± 0.8 μm	0.3-1.2 μm
Area	13.2 ± 3.03 μm^2	6.2–20.5 μm^2
Volume	7.92 ± 2.47 μm^3	1.86-24.6 μm^3
Volume of Acrosome	2.8 ± 0.606 μm^3	0.45–6.5 μm^3
Volume of Nucleus	5.1 ± 0.3 μm^3	1.4–18.2 μm^3

OSA CONTINUUM

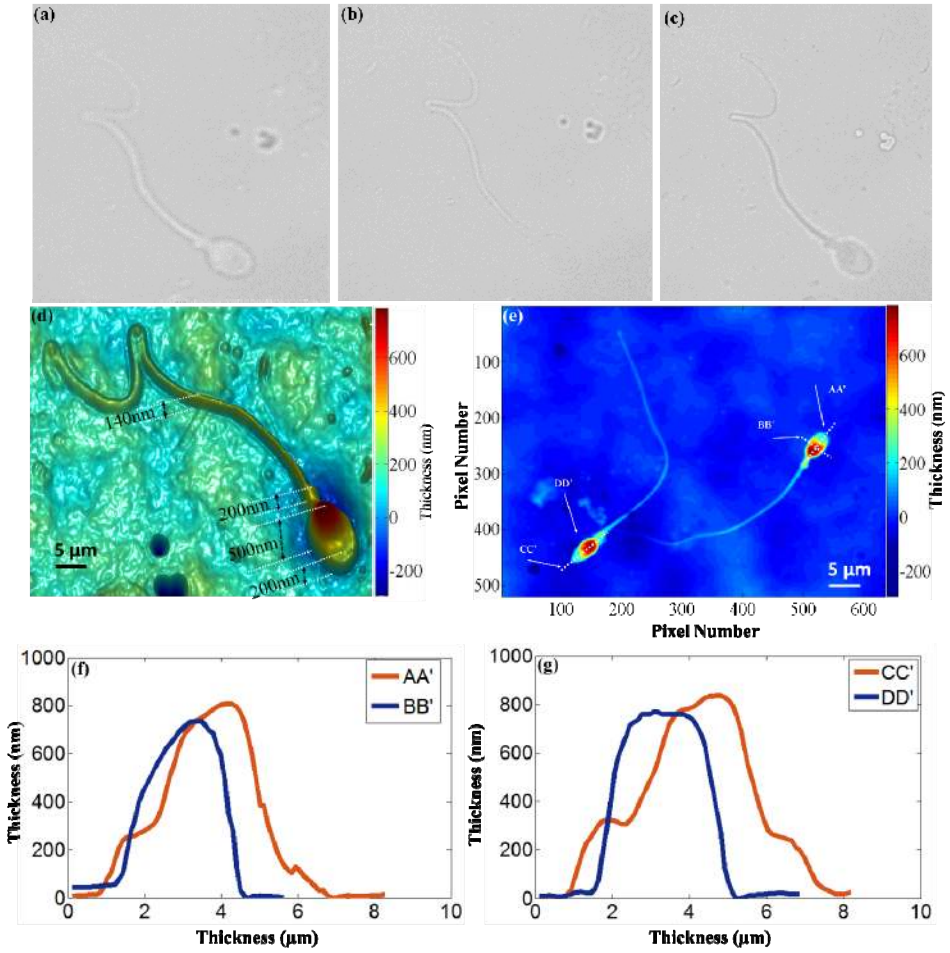

Fig. 2. Reconstruction of phase image of sperms in brightfield mode. (a-c) Brightfield images captured using the experimental set-up. (a) Image with a defocus of + 1 µm (b) Image in focus (c) Image with a defocus of −1 µm (d) Reconstructed phase image (e) 2D phase image of sperm cells (f) Quantitative profile of a spermatozoon along the line AA' and BB' shown in fig. (e), (g) Quantitative profile of a spermatozoon along the line CC' and DD' shown in fig. (e).

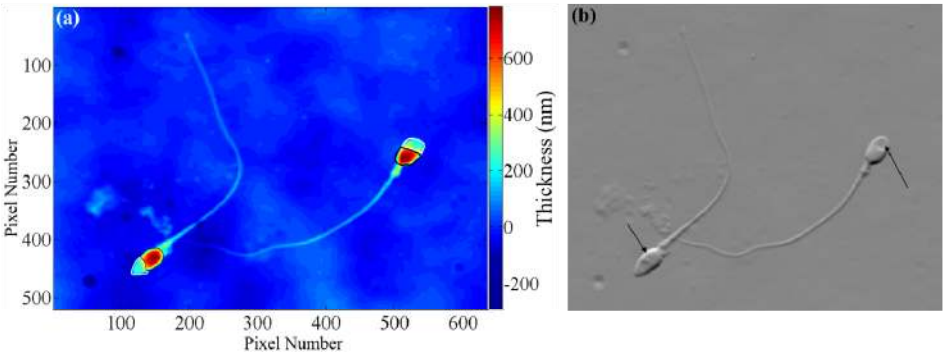

Fig. 3. (a) Compartmentalized sperm images, the black marked region is the nucleus and the yellow marked region is the acrosomal region in the reconstructed phase image. (b) Hilbert Transform operation enhanced nucleus and acrosome region. The arrows show vacuoles on the nucleus as well as on the acrosome region of sperm.

Experimental results show the high potential of TIE as a promising candidate for near-real time characterization of live spermatozoa without any sample preparations. The TIE imaging enables identification and quantification of anomalies (vacuoles, sperm head abnormalities) associated with the sperm cells as per WHO standards [14] as shown in Fig. 3(b). To identify the anomalies, we have applied TIE Hilbert transform approach [42] that will provide smoother phase images with edge enhancement of fine structures. The presence of vacuoles on the sperm head has been related to the poor outcomes in ART, increase in DNA fragmentation and abnormal chromatin packaging [56,58–60]. From the literature it was found that, spermatozoa with multiple vacuoles had loss of inner structural material of sperm head, so is its reduced volume distribution [55]. Preliminary imaging results of vacuolated spermatozoa and diffused nuclear region are suggestive of infertile spermatozoa. Hence this technique would find strong relevance in preferential selection of healthy spermatozoa based on the features leading to better outcomes in ICSI and IMSI procedures. However, detailed studies and clinical data are needed for conclusive prediction of integrity of normal viable spermatozoa [61–64]. TIE allows the possibility for a complete quantitative analysis of human spermatozoa in near-real time under a regular brightfield microscope and further sorting of cells according to specific morphological criteria that can be input to further processes related to ARTs without any interruption. We used the central wavelength 550 nm for calculation of the sample thickness. All the previous reports in literature take the mean central wavelength for phase and thickness calculations [55]. Errors in measurement based on the wavelength-dependent calculation of thickness are not accounted in this study. Another assumption that has been made in this manuscript is the constant refractive index of 1.35 [18]. This assumption is fairly accurate as per reported literature. Liu et al [57] have reported that the refractive index of the neck region reaches to values as high as 1.6 towards the head region and decreases towards the tail region down to 1.45 for a bovine sperm cell. However, after preliminary segmentation of nuclei, applying separate values of refractive indices to nuclear and cytoplasmic regions could improve the accuracy of volume estimations. Current studies reported in this manuscript on imaging speeds are only limited by the speed of the camera. By using a camera with higher frames rate, one will be able to easily quantify motility of spermatozoa along with the imaging and morphological analysis [65,66]. This helps in removing the motion artifacts and true real time reconstructions with GPUs.

We also report the results that illustrate the unique potential of TIE imaging in offering morphological information associated to the volume of DNA content of sperm cells. This imaging technique will be highly promising for real-time imaging of biological samples without any tedious pre-processing methods. It was reported in the literature [22,55], that there was no difference in the retrieved morphology of the stained and un-stained cells using a brightfield microscope. In most of the samples, more than 60% of spermatozoa with one or more vacuoles were found on the nucleus as well on the acrosomal region. The number of vacuoles per sperm ranged from 0 to 4 (mean: 2.01 ± 1.78).

6. Conclusion

In this paper, we have demonstrated a label-free method that can potentially be applied in clinical settings for selecting the potent spermatozoa for fertilization. The adopted TIE technique enables quantitative identification of the cellular organelles and their spatial distribution within the cell. Experimental results validate the capability of this technique in estimating the 3-D volume of spermatozoa with nanometric depth sensitivities. Being simple technique, TIE will help in evaluating the semen in resource-free settings in a cost effective manner without any special expertise. The feasibility to add the third dimension in spermatozoa analysis will provide a better understanding of the sperm behaviour and its relation with male infertility. We have shown that TIE can reveal the structural morphology of human spermatozoa in high resolution in an efficient manner compared to conventional qualitative microscopy techniques and interferometric techniques. Using TIE, we have

OSA CONTINUUM

evaluated the volume and precise location of vacuoles, and the volume of the nuclear content in sperm heads thus suggesting its use as a useful quantitative tool in assisted reproduction technologies. TIE is a viable tool for measuring the head volumes in presence as well as in absence of vacuoles. 3-D volume rendering of the spermatozoa helps in quick and accurate identification of various morphological anomalies that could be present in various regions of the spermatozoa. We have also identified separate cellular compartments (acrosome and nuclear compartments) in the retrieved phase maps of un-labelled spermatozoa cells. We anticipate that the extracted volume information using TIE will assist the clinicians in label-free selection of sperm cells for effective fertilization.

Funding

Science and Engineering Research Board (SERB), DST, India (SR/S2/LOP-0024/2012); Board of Research in Nuclear Sciences (BRNS), India (34/14/04/2015/BRNS).

Acknowledgments

Authors acknowledges Oasis Centre for Reproductive Medicine, Hyderabad, for providing Sperm samples. One of the authors, Dr. Renu John, acknowledges financial support from the Science and Engineering Research Board (SERB), DST, India (SR/S2/LOP-0024/2012) and Board of Research in Nuclear Sciences (BRNS), India (34/14/04/2015/BRNS).

Disclosures

The authors have no relevant financial interests in this article and no potential conflicts of interest to disclose.

References

1. National Research Council, "Biologic markers of human male reproductive health and physiologic damage," in *Biologic Markers in Reproductive Toxicolcology* (National Academy Press, 1989), pp. 83–106.
2. C. L. R. Barratt, S. Mansell, C. Beaton, S. Tardif, and S. K. Oxenham, "Diagnostic tools in male infertility-the question of sperm dysfunction," Asian J. Androl. **13**(1), 53–58 (2011).
3. T. Freour, A. Delvigne, and P. Barrière, "Evaluation of the male of the infertile couple," J. Gynecol. Obstet. Biol. Reprod. (Paris) **39**(8), S45–S52 (2010).
4. D. A. Paduch, "Testicular cancer and male infertility," Curr. Opin. Urol. **16**(6), 419–427 (2006).
5. J. D. Raman, C. F. Nobert, and M. Goldstein, "Increased incidence of testicular cancer in men presenting with infertility and abnormal semen analysis," J. Urol. **174**(5), 1819–1822 (2005).
6. D. S. Guzick, J. W. Overstreet, P. Factor-Litvak, C. K. Brazil, S. T. Nakajima, C. Coutifaris, S. A. Carson, P. Cisneros, M. P. Steinkampf, J. A. Hill, D. Xu, and D. L. Vogel; National Cooperative Reproductive Medicine Network, "Sperm morphology, motility, and concentration in fertile and infertile men," N. Engl. J. Med. **345**(19), 1388–1393 (2001).
7. W. Ombelet, K. Deblaere, E. Bosmans, A. Cox, P. Jacobs, M. Janssen, and M. Nijs, "Semen quality and intrauterine insemination," Reprod. Biomed. Online **7**(4), 485–492 (2003).
8. T. F. Kruger, A. A. Acosta, K. F. Simmons, R. J. Swanson, J. F. Matta, and S. Oehninger, "Predictive value of abnormal sperm morphology in in vitro fertilization," Fertil. Steril. **49**(1), 112–117 (1988).
9. B. Bartoov, A. Berkovitz, F. Eltes, A. Kogosowski, Y. Menezo, and Y. Barak, "Real-time fine morphology of motile human sperm cells is associated with IVF-ICSI outcome," J. Androl. **23**(1), 1–8 (2002).
10. G. Palermo, H. Joris, P. Devroey, and A. C. Van Steirteghem, "Pregnancies after intracytoplasmic injection of single spermatozoon into an oocyte," Lancet **340**(8810), 17–18 (1992).
11. M. Wilding, G. Coppola, L. di Matteo, A. Palagiano, E. Fusco, and B. Dale, "Intracytoplasmic injection of morphologically selected spermatozoa (IMSI) improves outcome after assisted reproduction by deselecting physiologically poor quality spermatozoa," J. Assist. Reprod. Genet. **28**(3), 253–262 (2011).
12. C. Garrett, D. Y. Liu, and H. W. Baker, "Selectivity of the human sperm-zona pellucida binding process to sperm head morphometry," Fertil. Steril. **67**(2), 362–371 (1997).
13. A. Berkovitz, F. Eltes, Y. Soffer, N. Zabludovsky, Y. Beyth, J. Farhi, D. Levran, and B. Bartoov, "ART success and in vivo sperm cell selection depend on the ultramorphological status of spermatozoa," Andrologia **31**(1), 1–8 (1999).
14. World Health Organization, "WHO laboratory manual for the examination and processing of human semen," (2010).
15. F. Zernike, "Phase contrast, a new method for the microscopic observation of transparent Objects," Physica **9**(7), 686–698 (1942).
16. W. Lang, *Nomarski Differential Interference-Contrast Microscopy* (Carl Zeiss, 1982).

OSA CONTINUUM

17. V. Centonze Frohlich, "Phase contrast and differential interference contrast (DIC) microscopy," J. Vis. Exp. **17**(17), e844 (2008).
18. G. Di Caprio, M. A. Gioffre, N. Saffioti, S. Grilli, P. Ferraro, R. Puglisi, D. Balduzzi, A. Galli, and G. Coppola, "Quantitative label-free animal sperm imaging by means of digital holographic microscopy," IEEE J. Sel. Top. Quantum Electron. **16**(4), 833–840 (2010).
19. G. Coppola, G. Di Caprio, M. Wilding, P. Ferraro, G. Esposito, L. Di Matteo, R. Dale, G. Coppola, and B. Dale, "Digital holographic microscopy for the evaluation of human sperm structure," Zygote **22**(4), 446–454 (2014).
20. G. Di Caprio, "Quantitative label-free cell imaging by means of digital holographic microscopy: a roadmap for a complete characterization of biological samples," (2011), unpublihsed.
21. I. Crha, J. Zakova, M. Huser, P. Ventruba, E. Lousova, and M. Pohanka, "Digital holographic microscopy in human sperm imaging," J. Assist. Reprod. Genet. **28**(8), 725–729 (2011).
22. M. Haifler, P. Girshovitz, G. Band, G. Dardikman, I. Madjar, and N. T. Shaked, "Interferometric phase microscopy for label-free morphological evaluation of sperm cells," Fertil. Steril. **104**(1), 43–47 (2015).
23. V. P. Pandiyan, K. Khare, and R. John, "Quantitative phase imaging of live cells with near on-axis digital holographic microscopy using constrained optimization approach," J. Biomed. Opt. **21**(10), 106003 (2016).
24. V. P. Pandiyan and R. John, "Optofluidic bioimaging platform for quantitative phase imaging of lab on a chip devices using digital holographic microscopy," Appl. Opt. **55**(3), A54–A59 (2016).
25. N. Lue, W. Choi, G. Popescu, T. Ikeda, R. R. Dasari, K. Badizadegan, and M. S. Feld, "Quantitative phase imaging of live cells using fast Fourier phase microscopy," Appl. Opt. **46**(10), 1836–1842 (2007).
26. T. Ikeda, G. Popescu, R. R. Dasari, and M. S. Feld, "Hilbert phase microscopy for investigating fast dynamics in transparent systems," Opt. Lett. **30**(10), 1165–1167 (2005).
27. G. Popescu, T. Ikeda, R. R. Dasari, and M. S. Feld, "Diffraction phase microscopy for quantifying cell structure and dynamics," Opt. Lett. **31**(6), 775–777 (2006).
28. Z. Wang, L. Millet, M. Mir, H. Ding, S. Unarunotai, J. Rogers, M. U. Gillette, and G. Popescu, "Spatial light interference microscopy (SLIM)," Opt. Express **19**(2), 1016–1026 (2011).
29. P. Bon, G. Maucort, B. Wattellier, and S. Monneret, "Quadriwave lateral shearing interferometry for quantitative phase microscopy of living cells," Opt. Express **17**(15), 13080–13094 (2009).
30. T. Kim, S. Sridharan, and G. Popescu, "Gradient field microscopy of unstained specimens," Opt. Express **20**(6), 6737–6745 (2012).
31. T. H. Nguyen, M. E. Kandel, M. Rubessa, M. B. Wheeler, and G. Popescu, "Gradient light interference microscopy for 3D imaging of unlabeled specimens," Nat. Commun. **8**(1), 210 (2017).
32. C. Zuo, Q. Chen, W. Qu, and A. Asundi, "Direct continuous phase demodulation in digital holography with use of the transport-of-intensity equation," Opt. Commun. **309**, 221–226 (2013).
33. A. Barty, K. A. Nugent, D. Paganin, and A. Roberts, "Quantitative optical phase microscopy," Opt. Lett. **23**(11), 817–819 (1998).
34. D. Paganin and K. A. Nugent, "Noninterferometric phase imaging with partially coherent light," Phys. Rev. Lett. **80**(12), 2586–2589 (1998).
35. N. Streibl, "Phase imaging by the transport equation of intensity," Opt. Commun. **49**(1), 6–10 (1984).
36. P. K. Poola, V. P. Pandiyan, V. Jayaraman, and R. John, "Quantitative label-free sperm imaging by means of transport of intensity," Proc. SPIE **9718**, 97180O (2016).
37. P. K. Poola, V. P. Pandiyan, and R. John, "Non-interferometric quantitative phase imaging of yeast cells," Proc. SPIE **9792**, 97920G (2015).
38. P. K. Poola and R. John, "Label-free nanoscale characterization of red blood cell structure and dynamics using single-shot transport of intensity equation," J. Biomed. Opt. **22**(10), 1–7 (2017).
39. K. Ishizuka and B. Allman, "Phase measurement of atomic resolution image using transport of intensity equation," J. Electron Microsc. (Tokyo) **54**(3), 191–197 (2005).
40. S. Bajt, A. Barty, K. A. Nugent, M. McCartney, M. Wall, and D. Paganin, "Quantitative phase-sensitive imaging in a transmission electron microscope," Ultramicroscopy **83**(1-2), 67–73 (2000).
41. K. A. Nugent, T. E. Gureyev, D. J. Cookson, D. Paganin, and Z. Barnea, "Quantitative phase imaging using hard x rays," Phys. Rev. Lett. **77**(14), 2961–2964 (1996).
42. W. S. Li, C. W. Chen, K. F. Lin, H. R. Chen, C. Y. Tsai, C. H. Chen, and W. F. Hsieh, "Phase retrieval by using the transport-of-intensity equation with Hilbert transform," Opt. Lett. **41**(7), 1616–1619 (2016).
43. M. R. Teague, "Deterministic phase retrieval: a Green's function solution," J. Opt. Soc. Am. **73**(11), 1434–1441 (1983).
44. M. R. Teague, "Image formation in terms of the transport equation," J. Opt. Soc. Am. A **2**(11), 2019–2026 (1985).
45. T. E. Gureyev, Ya. I. Nesterets, D. M. Paganin, A. Pogany, and S. W. Wilkins, "Linear algorithms for phase retrieval in the Fresnel region. 2. Partially coherent illumination," Opt. Commun. **259**(2), 569–580 (2006).
46. E. D. Barone-Nugent, A. Barty, and K. A. Nugent, "Quantitative phase-amplitude microscopy I: optical microscopy," J. Microsc. **206**(3), 194–203 (2002).
47. V. V. Volkov, Y. Zhu, and M. De Graef, "A new symmetrized solution for phase retrieval using the transport of intensity equation," Micron **33**(5), 411–416 (2002).
48. C. J. Bellair, C. L. Curl, B. E. Allman, P. J. Harris, A. Roberts, L. M. D. Delbridge, and K. A. Nugent, "Quantitative phase amplitude microscopy IV: imaging thick specimens," J. Microsc. **214**(1), 62–69 (2004).

OSA CONTINUUM

49. D. Paganin, A. Barty, P. J. McMahon, and K. A. Nugent, "Quantitative phase-amplitude microscopy. III. The effects of noise," J. Microsc. **214**(1), 51–61 (2004).
50. L. Waller, L. Tian, and G. Barbastathis, "Transport of Intensity imaging with higher order derivatives," Opt. Express **18**(12), 12552–12561 (2010).
51. C. Zuo, Q. Chen, and A. Asundi, "Boundary-artifact-free phase retrieval with the transport of intensity equation: fast solution with use of discrete cosine transform," Opt. Express **22**(8), 9220–9244 (2014).
52. J. Martinez-Carranza, K. Falaggis, and T. Kozacki, "Multi-filter transport of intensity equation solver with equalized noise sensitivity," Opt. Express **23**(18), 23092–23107 (2015).
53. C. Zuo, Q. Chen, Y. Yu, and A. Asundi, "Transport-of-intensity phase imaging using Savitzky-Golay differentiation filter--theory and applications," Opt. Express **21**(5), 5346–5362 (2013).
54. Z. Jingshan, R. A. Claus, J. Dauwels, L. Tian, and L. Waller, "Transport of Intensity phase imaging by intensity spectrum fitting of exponentially spaced defocus planes," Opt. Express **22**(9), 10661–10674 (2014).
55. M. Balberg, M. Levi, K. Kalinowski, I. Barnea, S. K. Mirsky, and N. T. Shaked, "Localized measurements of physical parameters within human sperm cells obtained with wide-field interferometry," J. Biophotonics **10**(10), 1305–1314 (2017).
56. J. G. Franco, Jr., R. L. R. Baruffi, A. L. Mauri, C. G. Petersen, J. B. A. Oliveira, and L. Vagnini, "Significance of large nuclear vacuoles in human spermatozoa: implications for ICSI," Reprod. Biomed. Online **17**(1), 42–45 (2008).
57. L. Liu, M. E. Kandel, M. Rubessa, S. Schreiber, M. B. Wheeler, and G. Popescu, "Topography and refractometry of sperm cells using spatial light interference microscopy," J. Biomed. Opt. **23**(2), 1–6 (2018).
58. J. G. Franco, Jr., A. L. Mauri, C. G. Petersen, F. C. Massaro, L. F. I. Silva, V. Felipe, M. Cavagna, A. Pontes, R. L. R. Baruffi, J. B. A. Oliveira, and L. D. Vagnini, "Large nuclear vacuoles are indicative of abnormal chromatin packaging in human spermatozoa," Int. J. Androl. **35**(1), 46–51 (2012).
59. J. P. Dadoune, "Expression of mammalian spermatozoal nucleoproteins," Microsc. Res. Tech. **61**(1), 56–75 (2003).
60. R. Mashiach, B. Fisch, F. Eltes, Y. Tadir, J. Ovadia, and B. Bartoov, "The relationship between sperm ultrastructural features and fertilizing capacity in vitro," Fertil. Steril. **57**(5), 1052–1057 (1992).
61. Y. Park, C. Depeursinge, and G. Popescu, "Quantitative phase imaging in biomedicine," Nat. Photonics **12**(10), 578–589 (2018).
62. M. U. Daloglu, W. Luo, F. Shabbir, F. Lin, K. Kim, I. Lee, J. Q. Jiang, W. J. Cai, V. Ramesh, M. Y. Yu, and A. Ozcan, "Label-free 3D computational imaging of spermatozoon locomotion, head spin and flagellum beating over a large volume," Light Sci. Appl. **7**(1), 17121 (2018).
63. M. Muschol, C. Wenders, and G. Wennemuth, "Four-dimensional analysis by high-speed holographic imaging reveals a chiral memory of sperm flagella," PLoS One **13**(6), e0199678 (2018).
64. W. Lee, J. H. Choi, S. Ryu, D. Jung, J. Song, J. S. Lee, and C. Joo, "Color-coded LED microscopy for quantitative phase imaging: Implementation and application to sperm motility analysis," Methods **136**, 66–74 (2018).
65. U. S. Kamilov, I. N. Papadopoulos, M. H. Shoreh, A. Goy, C. Vonesch, M. Unser, and D. Psaltis, "Learning approach to optical tomography," Optica **2**(6), 517–522 (2015).
66. L. Tian and L. Waller, "3D intensity and phase imaging from light field measurements in an LED array microscope," Optica **2**(2), 104–111 (2015).